A Water Monitoring System for Proton Exchange Membrane Fuel Cells Based on Ultrasonic Lamb Waves: An Ex Situ Proof of Concept

Zehua Dou, *Graduate Student Member, IEEE*, Bowen Fang, Laura Tropf, Harry Hoster, Hagen Schmidt, *Member, IEEE*, Jürgen Czarske, *Senior Member, IEEE*, and David Weik, *Graduate Student Member, IEEE*

***Abstract*— Up to date, the efficiencies of proton exchange membrane fuel cells (PEMFCs) are limited by the water flooding issue. Water monitoring systems, which are a crucial step to overcoming these flooding-related problems, are mostly either invasive or compromise on the temporal resolution and field of view. Thus, we propose an ultrasonic-Lamb-waves-based, real-time, and nondestructive water monitoring system. Briefly, ultrasonic transducers are mounted on the back side of bipolar plates (BPPs) exciting Lamb waves along flow channels incorporated in BPPs. Echo signals from water droplets in the channels are also received by the transducers. Thus, with the knowledge of Lamb wave propagation velocity, water droplets are spatially resolved by the time of flight of each droplet echo. Meanwhile, the energy of each droplet-induced echo wave packet is used to quantify the local flooding status. We have implemented a flexible and generic system adaptable to various flow field designs. The working principle was demonstrated for ex situ conditions with a BPP with a 25-cm^2 active area. A water sensitivity of at least 50 nL was realized, allowing for studying droplet and slug flows in PEMFCs. A 1.3-mm spatial resolution and a 2-kHz temporal resolution were simultaneously achieved. The high-performance water monitoring opens new horizons to study dynamic water evolution in channels of PEMFCs using cost-effective instrumentation, which may pave the way toward more efficient high-power PEMFCs with increased lifetimes.**

***Index Terms*— Cross correlation, echo localization, flooding issue, low-temperature proton exchange membrane fuel cell (PEMFC), ultrasonic flow field measurement, ultrasonic Lamb wave.**

Manuscript received 20 June 2023; revised 5 September 2023; accepted 17 October 2023. Date of publication 3 November 2023; date of current version 14 November 2023. This work was supported in part by the Confederation of Industrial Research Associations (AiF) through the Support Program "Industrial Joint Research" (IGF) of the German Federal Ministry of Economics and Technology under Grant 21151 BR and in part by the German Research Foundation DFG under Grant BU 2241/9-1 and Grant CZ55/43-2. The Associate Editor coordinating the review process was Dr. Chao Tan. *(Corresponding authors: Zehua Dou; David Weik.)*

Zehua Dou, Bowen Fang, Jürgen Czarske, and David Weik are with the Faculty of Electrical and Computer Engineering, Laboratory of Measurement and Sensor System Technique, Technische Universität Dresden, 01069 Dresden, Germany (e-mail: zehua.dou@tu-dresden.de; bowen.fang@mailbox.tu-dresden.de; juergen.czarske@tu-dresden.de; david.weik@tu-dresden.de).

Laura Tropf and Harry Hoster are with the Hydrogen and Fuel Cell Centre, ZBT GmbH, 47057 Duisburg, Germany (e-mail: L.Tropf@zbt.de; harry.hoster@uni-due.de).

Hagen Schmidt is with the Leibniz Institute for Solid State and Materials Research, 01069 Dresden, Germany (e-mail: h.schmidt@ifw-dresden.de).

Digital Object Identifier 10.1109/TIM.2023.3329101

I. Introduction

PROTON exchange membrane fuel cells (PEMFCs) are electrochemical devices that convert chemical energy into electricity, performing redox reactions of hydrogen and oxygen in a CO_2-emission-free process [1]. Specifically, low-temperature PEMFCs, which are operated below 100 °C, possess various attractive properties, namely, simple architecture [2], fast startup [3], and high power densities [4]. Thus, they show great potential to revolutionize energy resources for the next-generation automotive vehicles [5], portable devices [6], and stationary power storage systems [7]. However, during the operation of a PEMFC, water droplets are commonly formed as byproducts in its flow field, and the accumulation of water droplets may block the entire cross section of flow channels (Fig. 1) [8]. This hinders the gas (oxygen) transport and leads to an output power drop, which is termed as the flooding issue [9]. Aiming for PEMFCs with higher efficiency, knowledge of dynamic water generation and transportation behaviors during operation are of considerable importance [10]. This requires water monitoring systems that are capable of capturing the real-time water distribution—i.e., above 10 Hz—in an entire operating fuel cell and of providing sufficient spatial resolution to monitor local water transport phenomena in a nondestructive manner while using cost-effective infrastructure [11].

Up to date, various water monitoring systems for PEMFCs have been developed, including optical imaging [12], magnetic resonance imaging (MRI) [13], electrochemical impedance spectroscopy (EIS) [14], as well as radiography [15], computer tomography (CT), and small angle scattering exploiting X-rays and neutrons [16], [17], [18], [19]. Most of these techniques are able to provide high spatial resolutions ranging from sub-micrometer to sub-millimeter. However, they either exhibit serious drawbacks regarding cost, ease of access, and radiation damage in fuel cells [17] or suffer from the tradeoff between temporal resolution and the field-of-view (FoV) dimension. For example, optical visualization systems can only penetrate fuel cells with transparent bipolar plates (BPPs) [20], while MRI devices are not suitable for fuel cells with ferromagnetic materials [21]. Therefore, studies based on such systems are not representative for state-of-the-art PEMFCs with their carbon-based compound or metallic BPPs [22]. In X-ray

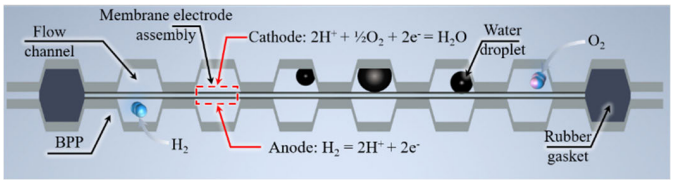

Fig. 1. Cross-sectional view of a typical PEMFC structure equipped with metallic BPPs, in which the working principle of PEMFCs and the water flooding issue is illustrated.

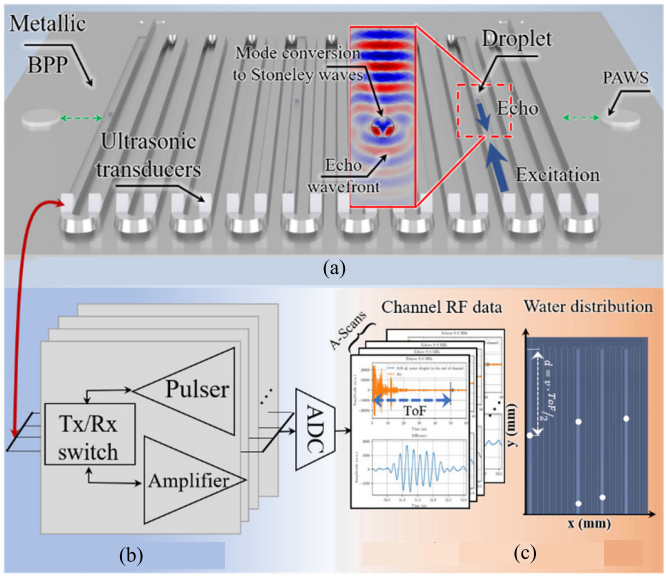

Fig. 2. Working principle of the proposed water monitoring system based on echo localization. (a) Lamb waves enable operando studies of water droplets in flow fields using ultrasonic transducers attached to the opposite side of monitored channels. Primary wave and echo propagate only along each flow channel (blue arrows). Inset: mechanism of droplet induced echo generation in the top view along a flow channel. Green arrows: wave propagation crossing the entire flow field proposed in [29] for comparison, where complicated reflections and mode conversions occur at each channel boundary. (b) Electronics: multichannel transceiver and data acquisition module. (c) Digital signal processing for localization and quantification of water droplets.

or neutron CT systems, the observation of water evolution phenomena in a PEMFC with separated water information of anode and cathode relies on the rotation of a test fuel cell and capturing 2-D radiographic images at various angles. Typical laboratory-based CT systems take more than an hour to acquire a single segmented water distribution of a small bespoke cell, e.g., with an active area of 2 cm^2 [23], which is insufficient to resolve dynamic water evolution occurring at the order of subseconds to seconds [24]. Higher image rates are only possible at synchrotron-based CT systems [25], which are more challenging to integrate into research and development work flows. The temporal resolution of EIS is limited to approximately 0.5 Hz mainly due to the investigated low-frequency range of typical 0.1 Hz–1 kHz [26].

Ultrasonic methods open new horizons to overcome these drawbacks. Up to date, the acoustic emission technique has been demonstrated for the diagnosis of water flooding in operating PEMFCs [27]: an ultrasonic transducer is directly coupled to a working PEMFC to receive longitudinal ultrasonic waves produced by water generation and removal. The accumulated acoustic emission energy correlates with the polarization state of test fuel cells [28]. Unfortunately, such a scheme of passively receiving ultrasonic waves is not able to spatially resolve water droplets, and therefore, it does not clearly reveal the dynamics of water generation, removal, and retention in a fuel cell. Moreover, the penetration depth of longitudinal waves in heterogeneous fuel cell structures is limited, which, in turn, reduces the FoV. In this regard, surface acoustic waves (SAWs) are superior thanks to their weak attenuation on plate-like structures—e.g., BPPs. Furthermore, the interaction of a SAW with a discontinuity on the surface, e.g., a droplet, will lead to reflection or attenuation of the incident wave [29]. In recent work, a tomographic water droplet localization scheme is implemented using Lamb waves crossing the entire flow field in different directions [30], in which a localization precision of approximately 4 mm in the case of a single 5-μL droplet was realized. The low sensitivity to water is mainly due to the low transmission efficiency of Lamb waves crossing the flow field with complicated geometries where reflections and mode conversions of Lamb waves are at rib-channel boundaries [green dashed arrows in Fig. 2(a)].

In this work, we propose a Lamb-wave-echo-localization based water monitoring system for PEMFCs (Fig. 2). In our approach, Lamb waves are only generated along flow channels where water droplets could appear using multiple ultrasonic transducers. Hence, the Lamb wave propagation along these free-standing flow channels can be approximated as a flat plate. Such an excitation scheme not only enhances the transmission efficiency of Lamb waves but also simplifies the localization procedure as multiple parallel A-scans of each flow channel [Fig. 2(c)]. It has been previously reported that droplets are echo-generic under Rayleigh–Lamb wave excitations, where an incident wave is a mode converted by a droplet to a Stoneley wave traveling along the three-phase contact line, which generates echoes [inset of Fig. 2(a)] [31], [32]. Thus, with a proper knowledge of the wave velocity, the position of a droplet can be accurately and precisely determined by resolving the time of flight (ToF) of a received echo. Moreover, as Lamb waves propagate along both surfaces of a plate-like carrier, water droplets sitting in a flow channel can be detected by ultrasonic transducers coupled to the opposite side of the BPP. Therefore, our proposed method requires only minimal modifications of PEMFC structures, which allows for nondestructive imaging of water droplets. Furthermore, the pulsed echo localization scheme provides high temporal resolution, thanks to fast wave velocities. In addition, our proposed system requires only ultrasonic transducers as well as a multichannel excitation and data acquisition device, which usually costs less than €20k. This drastically reduces the cost of systemic infrastructure compared with CT and MRI systems.

The remaining of this article is structured as follows. Section II demonstrates the detailed design and implementation of the water localization system, including the electronics and signal processing methods. The experimental

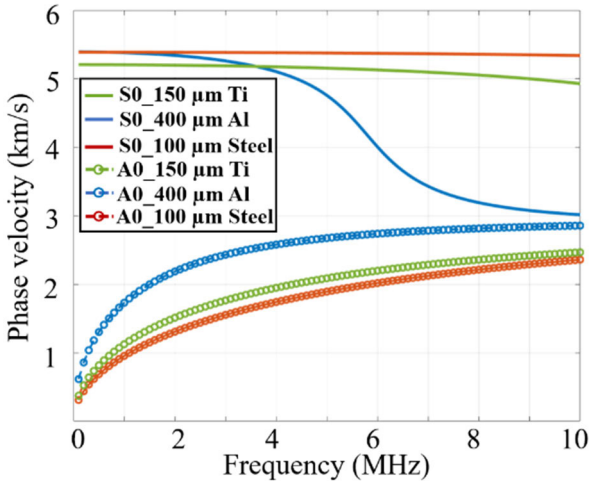

Fig. 3. Numerically calculated dispersion relations of fundamental Lamb modes for BPPs formed by three typical metals and thicknesses. The bulk wave velocities of the materials are taken from the material library of COMSOL Multiphysics [38].

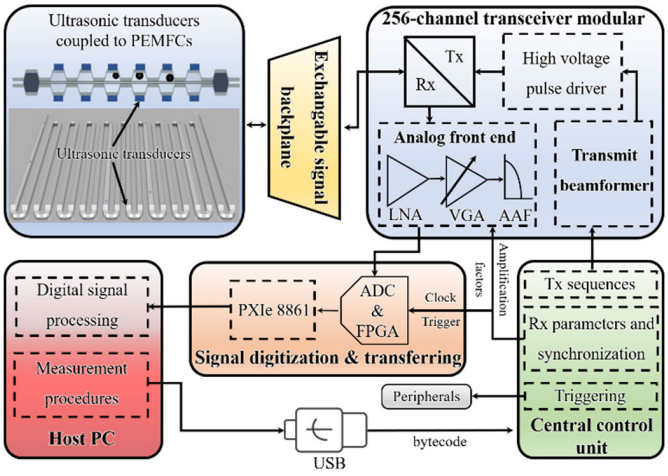

Fig. 4. Functional block diagram of the electronics.

setup and procedure are described in Section III. Section IV experimentally investigates the key performance metrics of the system in ex situ conditions, including the water sensitivity, spatiotemporal resolution, FoV, as well as accuracy and precision at quasi-static states. The results are analyzed and discussed in detail. Finally, the conclusions and outlook are summarized in Section V.

II. System Design and Implementation

A. Lamb Waves on BPPs

The basis of the proposed echo localization method is frequency-dependent phase velocities of Lamb waves on plate-like structures, i.e., dispersion relations, which are illustrated in Fig. 3. On a flat plate, the relation is determined by the thickness and the longitudinal and transverse wave velocities of the plate [33]. Metal and graphitic composite are the two main BPP materials for commercial PEMFCs. Metallic BPPs are superior in terms of high electrical and thermal conductivities, high mechanical strength, and low gas permeability [22], [34]. Metallic BPPs can be manufactured by stamp forming or hydroforming thin sheets of stainless steel, Aluminum (Al), Titanium (Ti), and their alloys [35]. BPP thicknesses range from 75 to 500 μm depending on the strengths of materials and the flow field designs [36]. In contrast, graphitic BPPs possess a wide range of compositions [37], and their filler matrix-based amorphous microstructures may lead to strong attenuation of acoustic waves. Therefore, they are not further discussed within this article.

For clarity, Fig. 3 shows the calculated phase velocities of the fundamental symmetric (S0) and antisymmetric (A0) plate modes of three typical metallic BPPs in the frequency range of 0.1–10 MHz. The temporal resolution of the pulsed echo localization scheme is determined by the double path Lamb wave propagation time along each flow channel. In this frequency range, both the S0 and A0 modes provide sufficiently high temporal resolution. For instance, a temporal resolution of 2 kHz can be achieved for large-scale PEMFCs, e.g., with 500-mm-long straight sections of flow channels, assuming a wave packet propagation velocity (i.e., the group velocity) of 2 km/s. Compared with the S0 modes, the slower A0 modes possess shorter wavelengths and potentially provide greater spatial resolution. Thus, only A0 modes are discussed within this work. Nevertheless, due to the similar A0 velocities in this frequency range, the aforementioned spatiotemporal resolution can generally be achieved for PEMFCs equipped with a wide variety of metallic BPPs.

Note that higher order Lamb modes with different velocities exist when the frequency-thickness product exceeds a certain value, which means that a single droplet may generate several echoes with different transient times leading to localization ambiguities. In this work, we realized pure A0 mode excitation and receiving with a gel-coupled angle beam transducer scheme to eliminate the potential localization ambiguity (details are given in Section III-A).

B. Multichannel Excitation and Data Acquisition System

As part of the proposed water monitoring system, our in-house built research platform serves as the excitation and data acquisition electronics that supports up to 256 simultaneous flow channels [39]. The modular electronics consists of three main parts, namely, a transceiver, a signal acquisition, and digitization module, and a central control unit, as shown in Fig. 4. Measurement procedures can be entered into the computer, such as the excitation waveform, pulse repetition frequency (PRF), receiver gain factors, sampling frequency, length of data acquisition events, and total measurement time. These given parameters are then interpreted into byte code by the Python-based host PC software, and executed by a 32-bit microcontroller (MCU) (ATSAM4SA16C, Atmel, USA).

Peripheral devices, such as optical cameras and gas compressors, can also be triggered by the MCU, allowing for synchronized operation. The transceiver circuit is capable of generating high voltage stimulations at PRF up to 20 kHz, to excite the ultrasonic transducers that are coupled to flow channels of BPPs. Interchangeable analog signal backplanes

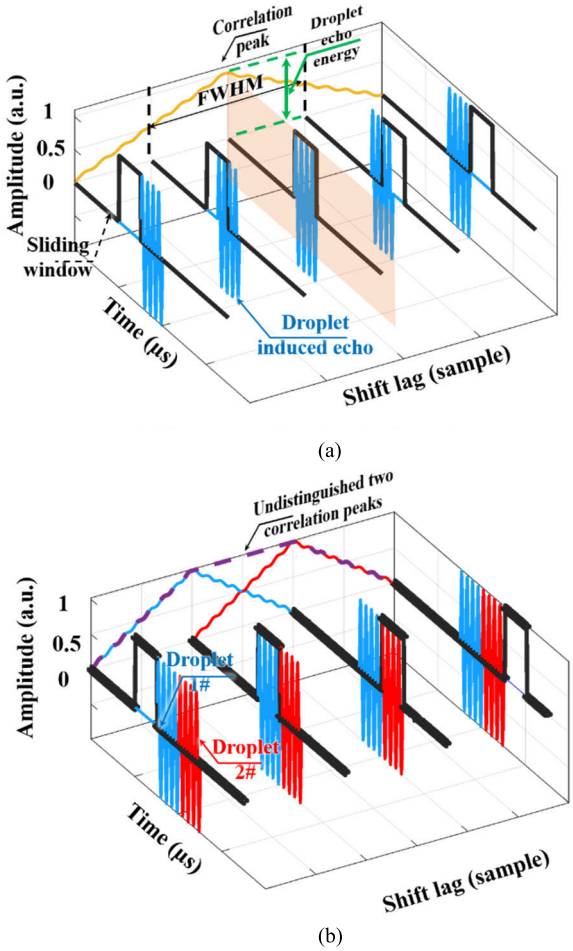

Fig. 5. Schematic of the cross-correlation-based signal processing method. (a) Physical interpretation of the cross-correlation method, where ToF and amplitude of a correlation peak are used to localize and quantify droplets. (b) Spatial resolution limit of the method corresponds to the FWHM of a cross-correlation peak.

are designed to connect the ultrasonic transducers and the transceiver circuitry, allowing probes with different interfaces or element mappings to be adapted to a variety of flow field designs and geometries.

The received and amplified echo signals are then digitized by analog-to-digital converters (ADC) (NI 5752, National Instruments, USA) with a sampling rate of up to 50 MHz at 12-bit digitization resolution. The digital signals are fed to field-programmable gate arrays (FPGAs) (PXIe-7965, NI), which can perform custom precondition, such as digital filtering and I/Q down conversion. Data are transferred to the host computer via PXI (PXIe-8861, NI) at a maximum rate of 8 GB/s, enabling real-time transfer of measurement data from large flow channels. Finally, the host PC performs digital signal processing to locate and quantify water content.

C. Quantification and Localization of Water Content

In this work, a cross-correlation technique is used to quantify and localize water droplets (Fig. 5), which is performed simultaneously for all flow channels. Specifically, the ultrasonic signals collected from linear time-invariant (LTI) flow channels are modeled as a superposition of reflected waves from different single droplets located at different positions and influenced by additive noise. Mathematically, this is written in (1), where the convolution of a transmitted signal $\mathrm{Tx}(t)$ and the Lamb mode shape-dependent reflection coefficient $r(t - 2 \cdot d/v)$ represents a complex Lamb wave reflection event from a droplet with a unit diameter whose center is at a distance of d from a transducer [29], v is the wave velocity, σ is the scattering cross section of the droplet, and $n(t)$ stands for additive noise

$$\mathrm{Rx}(t) = \sum \sqrt{\sigma} \cdot \mathrm{Tx}(t) \otimes r(t - 2 \cdot d/v) + n(t). \tag{1}$$

Thus, localization of a droplet requires resolving the transient time, i.e., ToF of its induced echo from a received signal. Moreover, (1) implies that the echo intensity is positively proportional to the dimension of a droplet. However, due to the complex 3-D geometry, an exact analytical expression of the reflection coefficient term in (1) is hard to obtain. Thus, the relation between echo energy and droplet dimension must be experimentally determined, and it enables a possibility to quantify the spatial water content, i.e., the local flooding status. More specifically, such a relationship provided by our measurement system applied to a specific BPP can be first experimentally characterized, and quantities of locally resolved water content in actual measurements can be estimated from the precalibrated relationship.

Therefore, the matched filter scheme is arguably the most suitable approach to simultaneously obtain the energy and ToF of each reflection event since it provides high signal-to-noise ratio (SNR). A matched filter performs a cross correlation of a received signal and a reference signal, where the latter is appropriately designed to match with actual measurement signals to a maximum extent [40]. Due to a lack of prior knowledge of the droplet-induced echo waveform, in this work, we combine the cross-correlation scheme and the echo signal energy integral method to accurately obtain both the droplet echo energy and its ToF [41]. This is realized by cross correlation of the square of a received signal and a unit rectangular window with the same duration of the excitation signal, as shown in Fig. 5(a)

$$\mathrm{rect} * \mathrm{Rx}^2[n] = \sum_{m=0}^{m=N} \mathrm{rect}[m - n] \cdot \mathrm{Rx}^2[m]. \tag{2}$$

This process is mathematically expressed as (2), in which rect and Rx are the unit rectangular function and the digitized received signal, possessing in total N samples indexed with m, respectively. Thus, the cross-correlation value calculated at each time shift n represents a sliding window energy of the received signal. With a sliding window length equal to the excitation duration, most of the droplet echo energy is concentrated at the beginning of the wavelet reception [orange area in Fig. 5(a)]. In other words, ToF and energy of the droplet echo can be accurately obtained by resolving the shift delay and amplitude of its cross-correlation peak, respectively. When locating multiple droplets with this approach, the correlation peaks of each droplet are superimposed in the output of the matched filter. Moreover, a ToF difference of two wavelets less

than their durations results in an overlapping of two correlation peaks so that they cannot be distinguished [Fig. 5(b)]. This means that the spatial resolution limit of this approach corresponds to the full-width at half-maximum (FWHM) of a correlation peak. Therefore, the highest spatial resolution that can be realized by this approach is on the order of wavelength for a single-period burst excitation, corresponding to a wider bandwidth in the frequency domain.

III. Experimental Methods

A. Measurement Setup and Parameters

For experimental validation purposes, a setup consisting of mainly four parts was assembled: a bespoke BPP, a linear ultrasonic transducer array, the system electronics, and a camera. To demonstrate the working principle of a representative BPP, the geometry and surface properties of the investigated BPP correspond to a simplified version of a state-of-the-art BPP design [43]. As depicted in Fig. 6(a), a flow field possessing a 20-bend single serpentine channel is incorporated into an Al BPP with a homogeneous sheet thickness of 400 μm. The total active area of the flow field is 25 mm^2, and the flow channel has a depth of 500 μm, a width of 1 mm, and a 50-mm length of each straight section. The measured water contact angle on this BPP was 63°. A linear ultrasonic transducer array (Imasonic SAS, 4-MHz central frequency, and 50% relative bandwidth) was coupled to a BPP from its backside [Fig. 6(b)] using ultrasound gel (SONOGLIDE FE 20). This configuration mimics operando monitoring of water evolution in the anode or cathode of a regular PEFMC without modifying its structure.

The transducer array possesses 128 elements with 0.95-mm length and a pitch of 300 μm between each two elements, which corresponds to a total active width of 38.4 mm covering the middle 16 straight sections of the serpentine except the inlet and outlet manifolds [red shade in Fig. 6(a)]. The active surface of the transducer array was aligned perpendicularly to the flow channels, ensuring the wave propagation along the straight sections of the flow channel. During measurements, only the elements attached to flow channels are activated. Moreover, due to the small element width, five elements are combined to detect water droplets in a single straight channel by summing up their received signals [Fig. 6(b)]. To generate and receive A0 mode Lamb waves, the incident angle of ultrasonic waves was adjusted to approximately 37°, according to Snell's law of the angled beam scheme (3). Specifically, v_{gel} and $v_{\text{p-A0}}$ in (3) are the phase velocities of longitudinal waves in the coupling gel and the A0 mode Lamb waves. Their values at 4 MHz, i.e., the central frequency of the transducer array, are estimated as 1540 and 2550 m/s, respectively,

$$\theta = \arcsin\left(v_{\text{gel}}/v_{\text{p-A0}}\right). \tag{3}$$

The experiments used single-cycle 4-MHz tone bursts with an amplitude of 100 V_{pp} at a PRF of 2 kHz to excite the ultrasonic transducers. Under such electrical excitations, the transducers generate approximately 1-μs pulses due to their 50% relative bandwidth. After transmission, the echo signals were recorded for 50 μs, corresponding to a single-path wave propagation distance over 60 mm, which is sufficient for detecting water droplets anywhere in the straight channels. The received echo signals were sampled at 50 MHz with 12-bit digitization resolution and bandpass filtered within the bandwidth of the transducer array.

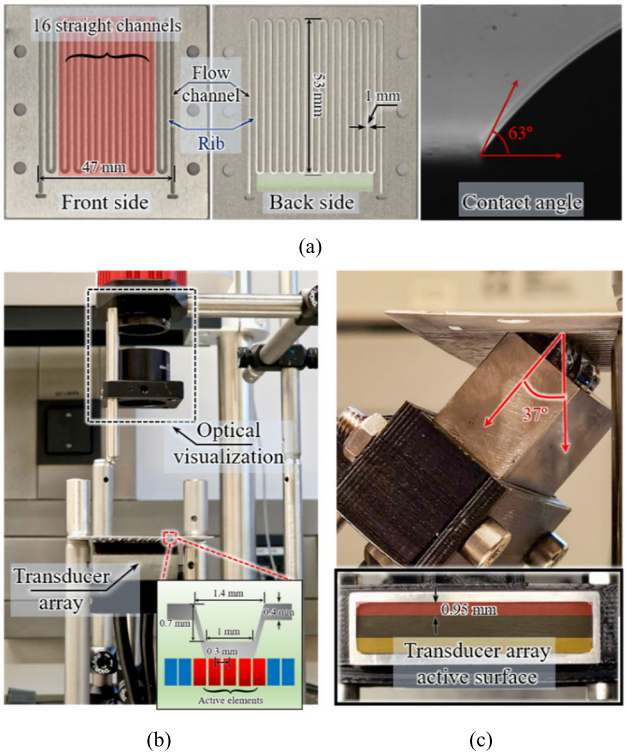

Fig. 6. Experimental setup (a) flow field geometry incorporated in 400-μm-thick Al BPPs; red and green shades indicate the monitored flow channels and position of transducer array, respectively, (b) bottom view of the setup, depicting cross-sectional dimensions of transducer array elements and flow channels, and (c) side view of angled beam transducer array (incident angle 37°). The transducer array possesses three separated element rows, and only the first row marked as red was used in the experiments.

A micropipette (TS-GP-01, Polypropylene) with a volume range of 100 nL–2.5 μL was used to manually apply tiny droplets into flow channels. This mimics water droplets' detachments from the gas diffusion layer (GDL) under a certain gas flow rate or confined by the channel depth [42]. The water content in flow channels and their actual positions were obtained from digital images recorded by a camera (Quantalux CS2100M-USB, Thorlabs) mounted above the BPP. With an FoV of the entire BPP, the camera provides a magnification factor of 25 pixels/mm. The proposed water monitoring system was investigated in our laboratory without additional temperature control.

B. Characterization Procedure

To be clear on the characterization procedure, Fig. 7(a) shows the two signals acquired before and after transferring a droplet into the same channel. It is observed that the actual droplet-induced echo is superimposed with electromagnetic interference (EMI) of the high voltage excitation and reverberations of longitudinal waves between the BPP and coupling gel surfaces. In order to accurately characterize

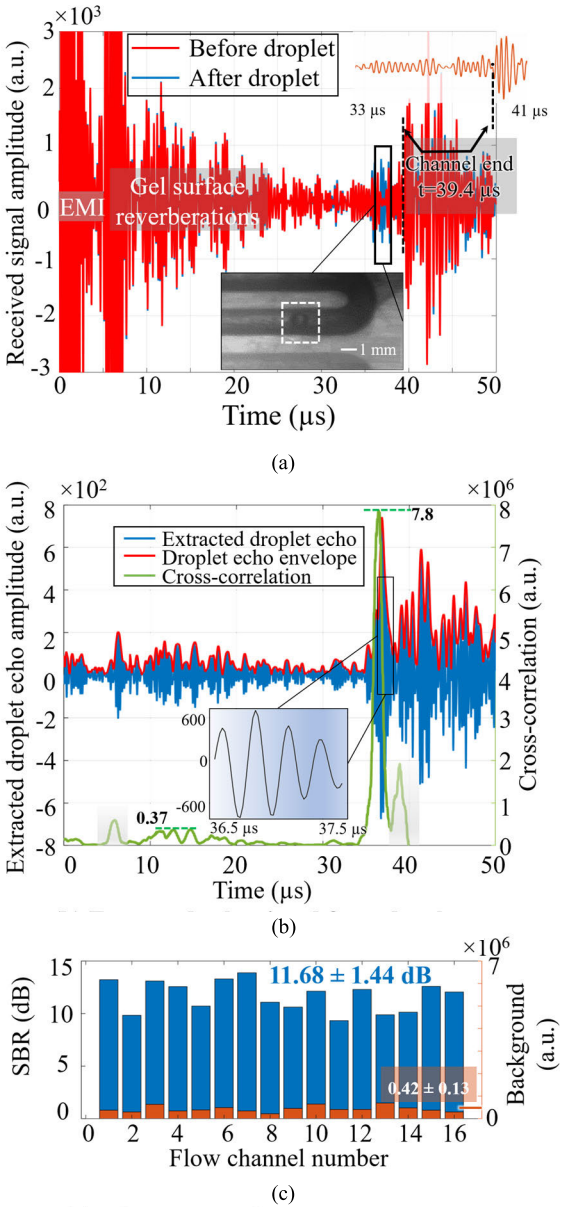

Fig. 7. Characterization on water sensitivity of the measurement system (a) two successive signals acquired before and after applying a droplet into the channel approximately 47.5 mm away from the transducer array (see inset); signal after digitization is provided in a.u. by the system, (b) extracted droplet-induced echo signal (blue line and inset), and cross-correlation values (green line) indicating the 50-point sliding window signal energy, and (c) SBR levels for resolving tiny droplets placed at the distal ends of all 16 straight channel sections covered by the transducer array, in which the highest background levels after baseline removal are also given.

the performance of our system monitoring water droplets, the droplet-unrelated background signal (baseline) must be properly removed from a signal measured with the presence of water droplets.

Because our manual operations of droplet transferring and wiping may occasionally lead to mechanical loose of the transducer array's fixture and deform the couplant gel, the droplet-unrelated baseline may vary over time. In this case, a simple subtraction of a sole baseline recorded beforehand in the absence of water droplets from a current-measured signal with droplets applied to a flow channel could lead to significant errors of the characterization [43], [44]. To mitigate such an issue, in our experiments, a new baseline was recorded right before transferring a droplet to a flow channel, and a subtraction was performed between the two measurements carried out one after the other together with droplet manipulations. This is known as a continuous baseline update and subtraction scheme that is widely applied in the field of structural health monitoring, in which this simple operation can effectively suppress gradual baseline variation due to, e.g., broad range 20 °C–60 °C temperature fluctuations [45]. This method is valid as long as the baseline difference between two measurements is negligible compared with the droplet-featured signals, which holds true in our ex- itu measurements. This is because droplets were abruptly applied to flow channels, and signals were acquired at a high repetition rate, during which time the baseline did not drastically change.

For further localization and quantification of water contents, an extracted droplet-induced echo signal was cross correlated with a unit rectangular function with a pulse duration of 1 μs (i.e., same as the excitation signal length) served as the reference signal.

IV. Results and Discussion

A. Sensitivity to Water Volume

We first determined the amount of water content that can be detected by our system. Considering the potential attenuation of Lamb waves with distance, the echo localization of water droplets that are placed at the distal end of each straight channel was investigated. Specifically, droplets with diameters smaller than the channel cross section were manually placed in the channels at approximately 47.5 mm from the transducer array [inset of Fig. 7(a)]. It is worth mentioning that the volumes of these droplets were below the precision limit (100 $\pm$ 15 nL) of the micropipette. Therefore, the actual volumes of droplets transferred into flow channels were estimated from their diameters captured in the digital images together with the contact angle, as 50 $\pm$ 15 nL.

For the particular case shown in Fig. 7(a), the extracted droplet-induced echo and the cross-correlation values are plotted in Fig. 7(b), where the high amplitude wave packet onset at 36.5 μs is clearly observed and indicated by the position of the highest cross-correlation peak. It is noticed that the signal starting from 39.4 μs (appearing both in the baseline and in the measurement) represents the reflection from the end of the channel, which provides a real-time updated estimation on the group velocity of the wave packet

$$V_g = 2 \times 51.5 \text{ mm}/39.4\ \mu\text{s} = 2614.2 \text{ m/s}. \tag{4}$$

Hence, the center of the droplet is calculated at $d = V_g \cdot \Delta t/2 = 47.71$ mm away from the transducer array, in very good agreement with the optically resolved 47.5 mm.

Moreover, the ability of the cross-correlation method to accurately and precisely distinguish a droplet from background noise with baseline removed is represented as the ratio of the droplet echo energy and the highest energy of background

noise in 1 μs, which is termed here as the signal-to-background ratio (SBR). For the particular case shown in Fig. 7(a) and (b), the SBR value is calculated in terms of echo energies (5), neglecting the first reflection from coupling gel surface and the echo from the end of channel

$$\mathrm{SBR} = 10 \cdot \log_{10}(7.8/0.37) = 13.24\ \mathrm{dB}. \tag{5}$$

Similarly, the SBR and background levels provided by our measurement system monitoring a tiny droplet appearing at the distal ends of all investigated channel sections were investigated and plotted in Fig. 7(c). This achieved SBR with a mean value of 11.68 dB and a standard deviation of 1.44 dB proves that our system is capable of localizing water droplets as small as 50 nL, and the realized high SBR levels suggest that the sensitivity limit of our system could be higher than this value. Nevertheless, the background levels are comparable among the monitored 16 flow channel sections providing a mean value as low as $(0.42 \pm 0.13) \times 10^6$, which indicates the effectiveness of the continuous baseline scheme and the consistency of our measurement system across the entire FoV. While the fluctuations of the SBR levels are mainly attributed to the echo energy of droplets with slightly different volumes.

B. Quantification of the Local Water Content

For the purpose of evaluating local water content, the relations of echo energy and the volume and the position of the droplets were characterized. These experiments were carried out only for one straight channel due to the consistency of our measurement system. We studied water droplets with three different volumes: 175 ± 25, 100 ± 15, and 50 ± 15 nL. The insets of Fig. 8(a) depict optical images of a flow channel containing such droplets. A 50-nL droplet only partially occupies the flow channel cross section, representative for droplet flows commonly observed in PEMFCs operated at high current densities [46]. In contrast, droplets beyond 100 nL entirely clog the flow channel, which represents slug/plug flows that reduce the output power of PEMFCs [47].

The influence of the droplet position and volume on its echo energy was obtained from measurements of 24 different droplets. They were placed at different positions in a flow channel, and the droplet position and volume dependencies of echo energy are plotted in Fig. 8(a) and (b), respectively. First, Fig. 8(a) shows that the echo energy is not clearly correlated with the position of the droplet in all liquid volume groups, where energies from near and far droplets in the same volume group are comparable. This can be explained by the low attenuation of Lamb waves on metallic BPPs. In contrast, a strongly positive correlation between echo energy and droplet dimension is observed. The average value of echo energy was four times increased, when the liquid volume increased from 50 to 100 nL. Further increasing the water volume to approximately 175 nL, i.e., forming an elliptical slug in the channel, does not affect the echo energy much. This is because a droplet of approximately 100 nL fully occupies the entire channel width, and the scattering cross section of a bigger slug cannot be further increased. Therefore, the received echo energy is saturated at this level.

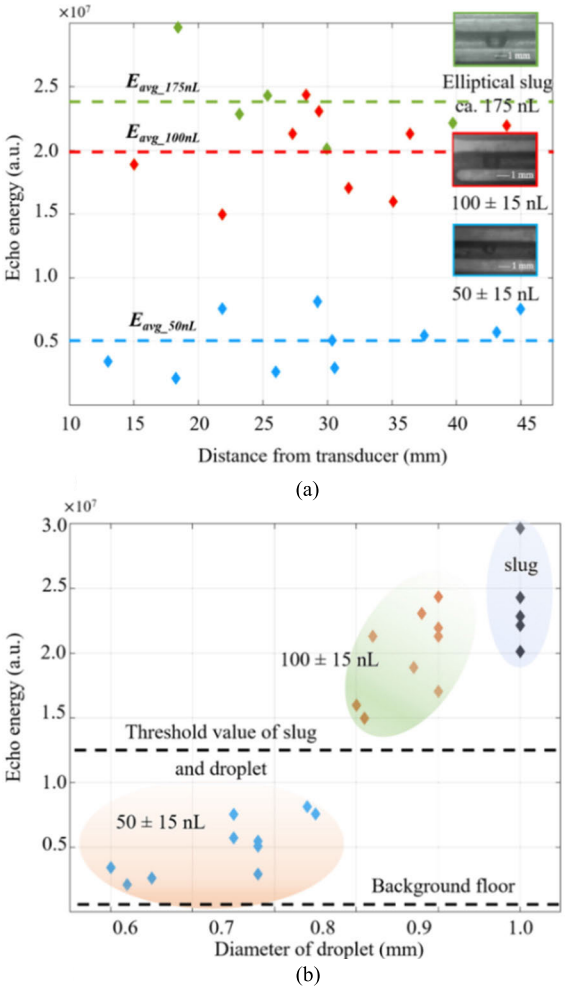

Fig. 8. Relations of echo energy, droplet volume, and position from 24 droplets placed at various positions in a flow channel, allowing for evaluation of local flooding status. (a) Relation of echo energy and position of droplet with three different volumes. (b) Relation of echo energy and droplet diameter.

Insufficient liquid volume control and optical imaging resolution prohibited us from deriving a physically meaningful relation of droplet dimension and resulting echo energy. Nanoliter level precision might, otherwise, be possible by curve fitting of the measured data [48]. Nevertheless, the local flooding status of a flow channel can be determined in a semiquantitative manner, setting two threshold values: a spatially resolved reflection event with echo energy greater than 1.25×10^7 is considered a "slug," and any other received echo energy higher than the background floor counts as "partially wetted."

C. Localization Accuracy

In experiments, the local background noise interferes with the droplet-induced echo, which may lead to localization error due to a correlation peak shift of multiple sampling points. In order to evaluate the accuracy of our system, the absolute values of localization errors for the group of 50 ± 15 nL droplets placed at different positions in a flow channel are plotted in Fig. 9, in which the background color is encoded

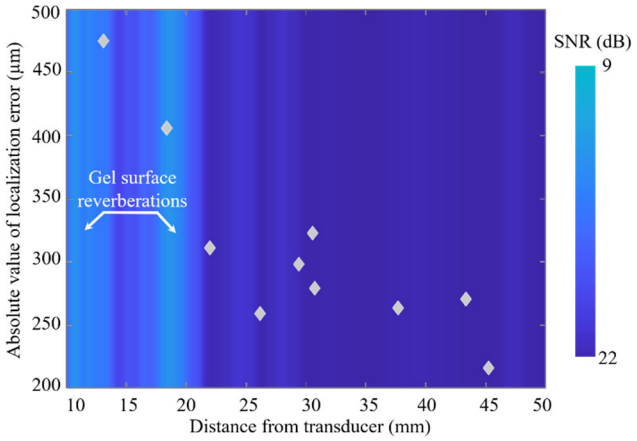

Fig. 9. Relation of the absolute values of localization errors, position, and local SNRs for the group of 50 ± 15 nL droplets.

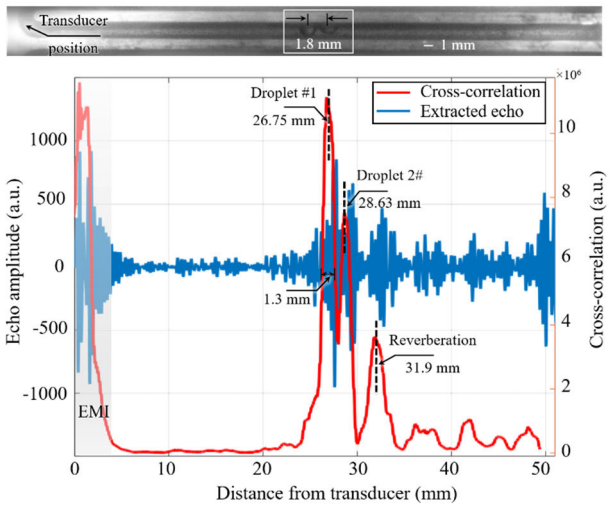

Fig. 10. Measurement of the spatial resolution of the cross-correlation localization scheme.

by the local SNR values. Note that the local the SNR values here are different from the aforementioned SBR. This is because the background noise level is position dependent. The background noise exhibits a higher amplitude in closer distances that correspond to multiple reflections from the gel wedge surface [see Figs. 7(b) and 9]. This phenomenon appeared in the acquired signals of all droplets. This makes the abovementioned SBR value indicating the overall detectability unsuitable to evaluate local noise interfering with a droplet echo at the same time gate. To obtain the local SNRs, the mean value of these measured droplets' echo energy is used as the signal level, i.e., 5.06×10^7 (see Fig. 8), while the noise level of each position integrates the noise energy over a 1-μs window in the corresponding time gate, and the noise signal is taken from the baseline variation measured in the absence of droplets.

In Fig. 9, a negative correlation between localization error and local SNR is clearly observed. And, the localization errors at 13.1 and 18.4 mm were induced by the gel wedge, which can be improved by using a regular non-destructive testing (NDT) wedge with a damping layer [49]. Moreover, the localization errors of all 50 nL small droplets are all within 500 μm that is below one wavelength. In contrast, due to the high echo energy of the other two groups of bigger droplets, their localization errors were all within 200 μm at any place in the flow channel, with SNRs higher than 16 dB.

D. Spatiotemporal Resolution

The spatial resolution, as a key performance metric of the water monitoring system, was further investigated. For this purpose, two water droplets were placed close to each other in the same flow channel, as shown in Fig. 10. From the optical image, the distance between the centers of the two droplets is measured as 1.8–1.9 mm. The measured echo signal with baseline subtracted is also plotted in Fig. 10, together with the cross-correlation result. Taking the group velocity calculated in (4), the two droplets are more clearly resolved at 26.75 and 28.63 mm from the transducer, respectively. Thus, their distance obtained in the ultrasonic measurement is 1.88 mm, in good agreement with the optical measurement. It is noticed that, with the given excitation parameters, the resulting FWHM of the correlation peak is 1.3 mm, which is the spatial resolution limit of the cross-correlation approach. In practical experiments, with a center distance below approximately 1.5 mm, two nearby slugs or relatively bigger droplets approximately 100 nL soon merge with each other due to the surface tension. Therefore, the current spatial resolution is sufficient to study the dynamic droplet evolution in PEMFCs. Furthermore, the echo energy of both droplets is below the threshold value of slug flow set at 1.25×10^7. Therefore, the flow channel at the two positions is determined as partially wetted, which agrees well with the optical image as well. The ratio of the two correlation peak amplitudes, i.e., the echo energy, also stands for their relative dimensions. However, in addition to the two high amplitude peaks, another peak with a lower amplitude corresponding to 31.9 mm appears, whereas no droplet was observed there in the flow channel. We propose that this may be a pseudo-peak due to the reverberation, i.e., a secondary echo traveled twice the distance between the two droplets.

E. Comparison to Other Techniques

Table I positions our proposed method in the field of available techniques, including state-of-the-art imaging-based X-ray and neutron CT systems, as well as nonimaging EIS. Compared with CT systems, our approach scores in cost effectiveness, ease of availability, and flexible adaption, and it is not limited by the tradeoff between temporal resolution and FOV. In contrast, the CT systems are superior with respect to sensitivity to water and spatial resolution, and also in monitoring the MEA. EIS is another cost effective and noninvasive diagnosis method for PEMFCs. EIS is capable of detecting air starvation, membrane dehydration, and water flooding, which outperforms other techniques listed in Table I that are dedicated only for water monitoring. However, most EIS systems emphasize on global fault diagnosis of PEMFCs, and therefore, they are hardly able to localize the fault sites.

TABLE I
COMPARISON OF KEY PERFORMANCE METRICS FOR SELECTED WATER MONITORING METHODS

	This work	X-CT [16]	Neutron CT [17]	EIS [26]
Costs and availability	Low cost with flexible designs	Costly devices	Only on-site measurements possible	Cost effective and widely performed
Destruction	No or minimal modification required	Potential degradation to FC components [50]	Moderate modifications required	Noninvasive (except localized EIS [51])
Sensitivity to water	10's of nL	Sub-nL level	nL level	N/A
Spatiotemporal resolution & FOV	1.3 mm @ 2 kHz; 25 cm^2	0.4 µm @ 4 Hz; 2.56 mm^2	63.6 µm @ 0.025 Hz; 2 cm^2	No spatial resolution; low temporal resolution ~ 0.01 Hz
Other comments	Not yet able to access MEA water contents	More insights on MEA water contents	Potential penetration depth limits studying stack structures	Capable of fault detecting, including starvation, membrane dehydration and water flooding

Therefore, EIS might not provide sufficient insights on flow field optimization toward advanced water management of PEMFCs.

V. CONCLUSION AND OUTLOOK

In this work, we presented a novel ultrasonic Lamb-wave-based water monitoring system for PEM fuel cells. Our ex situ experiments show that the proposed system is able to accurately localize water volumes within research and development scale PEMFC flow fields with high spatiotemporal resolution at quasi-static states.

First, mimicking droplet detachment into flow channels using a manual micropipette, we demonstrated that our system is able to detect a water volume of 50 nL in the entire 50-mm-long straight sections of the flow field. We emphasize that the determined sensitivity to water content does not correspond to the lower limit of our instrumentation but rather of the precision limit of our volume control. Together with the continuous baseline update and subtraction scheme suppressing slow variations of the system like mechanical loss, our system is able to clearly discriminate such 50-nL droplets providing high SBR over 10 dB.

Second, a spatial resolution of 1.3 mm for localizing droplets was achieved by a cross correlation-based ToF ranging method, which is sufficient for studying the generation and accumulation of 50-nL droplets. Meanwhile, three flooding states can be distinguished from the strength of a measured echo signal, i.e., its cross-correlation peak height, namely, dry, partially wetted (approximately 50 nL), and fully clogged (>100 nL).

The use of a real-time Lamb wave velocity estimation from the end-of-channel reflection allowed us to accurately localize droplets that were abruptly transferred into flow channels, where the localization errors were less than 500 μm.

One of the main advantages of the proposed method is the temporal resolution in the kilohertz range. This provides us with sufficient flexibility to scale up our current instrumentation for applications in technical fuel cells with larger dimensions and more complex flow field designs. This can be realized by integrating more compact ultrasonic transducers to all flow channels, and the transducers can be accessed by a time-division multiplexing scheme without further increasing more simultaneous channels of the transceiver circuit.

In summary, given the geometry of the BPP, sensitivity, spatiotemporal resolution, and FoV, our proposed method is sufficient for monitoring water evolution not only in research and development scale PEMFCs, and the results also suggest a transferability of the method to technically relevant sizes. The work shown here is a proof of concept of the proposed Lamb-wave-based echo localization of water droplets method, and it serves as a performance benchmark for future developments. In situ/operando demonstrations of the system are certainly the next step for the method on the path to an application breakthrough. However, they would require more complicated instrumentations and measurement procedures, e.g., to integrate a test cell instrumented by our system with an X-ray microscopy that can penetrate the opaque cell and provide references for our system. This is a first priority of our future studies and is, therefore, beyond the scope of the presented work. Future refinements of the method should include several aspects.

1) Nonstraight sections of the flow field can be monitored using longitudinal waves exploring acoustic impedance mismatching at the BPP-water interface [52].
2) Exploring the lower sensitivity limits for droplet volumes smaller than 50 nL, which will be needed for PEMFC operation at higher flow rates or dry conditions [42]. For better resolving such smaller droplets, further improvements on spatial resolution could be realized by, e.g., Richardson–Lucy deconvolution-based ultrasound localization microscopy (ULM) algorithms [53], and its performance can be further enhanced by machine learning techniques especially in noisy PEMFC operating conditions [54].
3) Further in situ experiments should explore different environmental and operational conditions (EOCs) relevant for technical PEMFCs, e.g., for automobiles and stationary power plants, where the temperature fluctuates at minute level or longer around 60 °C [55], [56], and vibrations of BPPs may occur at tens of hertz [57], [58]. The performance of state-of-the-art EOC compensation methods, e.g., singular value decomposition (SVD) combined and K-means clustering [59], will be comprehensively evaluated using

large datasets recorded by our system to ensure their general effectiveness and reliability in real applications.

4) Toward integrating our measurement system with technical fuel cell systems, compact piezoelectric material-based interdigitated ultrasonic transducers (IDTs) that can be permanently installed to the back side of each flow channel incorporated in BPPs will be further implemented and optimized toward high sensitivities. A single cell equipped with such IDTs then serves as a test unit that can be inserted anywhere in a PEMFC stack for studying local water evolution behaviors that may be influenced by the assembly pressure and current distribution inside the stack.

Our future research will, thus, focus on addressing these aspects and demonstrating operando water monitoring using ultrasonic Lamb waves.

ACKNOWLEDGMENT

The authors would like to thank H. Emmerich and J. Gürtler for valuable discussions, as well as C. Bilsing and F. Bürkle for their help on optical measurements. They would also like to thank L. Büttner for connecting collaborations between TU Dresden, Dresden, Germany, and the Hydrogen and Fuel Cell Centre, ZBT GmbH, Duisburg, Germany, over the years. The general laboratory assistance by C. John and J. Matzke are greatly appreciated.

Data Availability: The authors declare that all data supporting the findings of the study are available within this article.

REFERENCES

[1] O. Z. Sharaf and M. F. Orhan, "An overview of fuel cell technology: Fundamentals and applications," *Renew. Sustain. Energy Rev.*, vol. 32, pp. 810–853, Apr. 2014, doi: 10.1016/j.rser.2014.01.012.

[2] P. C. Okonkwo et al., "Platinum degradation mechanisms in proton exchange membrane fuel cell (PEMFC) system: A review," *Int. J. Hydrogen Energy*, vol. 46, no. 29, pp. 15850–15865, Apr. 2021, doi: 10.1016/j.ijhydene.2021.02.078.

[3] A. Parekh, "Recent developments of proton exchange membranes for PEMFC: A review," *Frontiers Energy Res.*, vol. 10, Sep. 2022, Art. no. 956132, doi: 10.3389/fenrg.2022.956132.

[4] N. Bussayajarn, H. Ming, K. K. Hoong, W. Y. Ming Stephen, and C. S. Hwa, "Planar air breathing PEMFC with self-humidifying MEA and open cathode geometry design for portable applications," *Int. J. Hydrogen Energy*, vol. 34, no. 18, pp. 7761–7767, Sep. 2009, doi: 10.1016/j.ijhydene.2009.07.077.

[5] B. G. Pollet, S. S. Kocha, and I. Staffell, "Current status of automotive fuel cells for sustainable transport," *Current Opinion Electrochemistry*, vol. 16, pp. 90–95, Aug. 2019, doi: 10.1016/j.coelec.2019.04.021.

[6] J. Fernández-Moreno, G. Guelbenzu, A. J. Martín, M. A. Folgado, P. Ferreira-Aparicio, and A. M. Chaparro, "A portable system powered with hydrogen and one single air-breathing PEM fuel cell," *Appl. Energy*, vol. 109, pp. 60–66, Sep. 2013, doi: 10.1016/j.apenergy.2013.03.076.

[7] S. V. Mitrofanov, N. G. Kiryanova, and A. M. Gorlova, "Stationary hybrid renewable energy systems for railway electrification: A review," *Energies*, vol. 14, no. 18, p. 5946, Sep. 2021, doi: 10.3390/en14185946.

[8] P. K. K. Bhattacharya, "Water flooding in the proton exchange membrane fuel cell," *Directions*, vol. 15, no. 1, pp. 24–33, 2015. [Online]. Available: https://www.sciencetheearth.com/uploads/2/4/6/5/24658156/waterflooding_protonexchangemembrane.pdf

[9] H. Li et al., "A review of water flooding issues in the proton exchange membrane fuel cell," *J. Power Sources*, vol. 178, no. 1, pp. 103–117, Mar. 2008, doi: 10.1016/j.jpowsour.2007.12.068.

[10] X. R. Wang, Y. Ma, J. Gao, T. Li, G. Z. Jiang, and Z. Y. Sun, "Review on water management methods for proton exchange membrane fuel cells," *Int. J. Hydrogen Energy*, vol. 46, no. 22, pp. 12206–12229, Mar. 2021, doi: 10.1016/j.ijhydene.2020.06.211.

[11] A. Bazylak, "Liquid water visualization in PEM fuel cells: A review," *Int. J. Hydrogen Energy*, vol. 34, no. 9, pp. 3845–3857, May 2009, doi: 10.1016/j.ijhydene.2009.02.084.

[12] K. Nishida, R. Taniguchi, Y. Ishizaki, S. Tsushima, and S. Hirai, "Impacts of channel wettability and flow direction on liquid water transport in the serpentine flow field of a polymer electrolyte fuel cell," *J. Power Sources*, vol. 275, pp. 447–457, Feb. 2015, doi: 10.1016/j.jpowsour.2014.11.059.

[13] Z. W. Dunbar and R. I. Masel, "Magnetic resonance imaging investigation of water accumulation and transport in graphite flow fields in a polymer electrolyte membrane fuel cell: Do defects control transport?" *J. Power Sources*, vol. 182, no. 1, pp. 76–82, Jul. 2008, doi: 10.1016/j.jpowsour.2008.03.057.

[14] P. Jiang, J. Chen, L. Jin, and L. Kumar, "Adaptive condition monitoring for fuel cells based on fast EIS and two-frequency impedance measurements," *IEEE Trans. Ind. Electron.*, vol. 70, no. 8, pp. 8517–8525, Aug. 2023, doi: 10.1109/tie.2022.3220843.

[15] I. Manke et al., "Investigation of water evolution and transport in fuel cells with high resolution synchrotron X-ray radiography," *Appl. Phys. Lett.*, vol. 90, no. 17, Apr. 2007, Art. no. 174105, doi: 10.1063/1.2731440.

[16] H. Xu et al., "(Invited) exploring sub-second and sub-micron X-ray tomographic imaging of liquid water in PEFC gas diffusion layers," *ECS Meet. Abstr.*, vol. 2, p. 1406, Jul. 2019, doi: 10.1149/ma2019-02/32/1406.

[17] R. F. Ziesche et al., "High-speed 4D neutron computed tomography for quantifying water dynamics in polymer electrolyte fuel cells," *Nature Commun.*, vol. 13, no. 1, pp. 1–11, Mar. 2022, doi: 10.1038/s41467-022-29313-5.

[18] C. Tötzke et al., "Large area high resolution neutron imaging detector for fuel cell research," *J. Power Sources*, vol. 196, no. 10, pp. 4631–4637, May 2011, doi: 10.1016/j.jpowsour.2011.01.049.

[19] G. Gebel, O. Diat, S. Escribano, and R. Mosdale, "Water profile determination in a running PEMFC by small-angle neutron scattering," *J. Power Sources*, vol. 179, no. 1, pp. 132–139, Apr. 2008, doi: 10.1016/j.jpowsour.2007.12.124.

[20] F. Bürkle et al., "Investigation and equalisation of the flow distribution in a fuel cell stack," *J. Power Sources*, vol. 448, Feb. 2020, Art. no. 227546, doi: 10.1016/j.jpowsour.2019.227546.

[21] M. Ji and Z. Wei, "A review of water management in polymer electrolyte membrane fuel cells," *Energies*, vol. 2, no. 4, pp. 1057–1106, Nov. 2009, doi: 10.3390/en20401057.

[22] A. Tang, L. Crisci, L. Bonville, and J. Jankovic, "An overview of bipolar plates in proton exchange membrane fuel cells," *J. Renew. Sustain. Energy*, vol. 13, no. 2, Mar. 2021, doi: 10.1063/5.0031447.

[23] J. Hack et al., "Use of X-ray computed tomography for understanding localised, along-the-channel degradation of polymer electrolyte fuel cells," *Electrochimica Acta*, vol. 352, Aug. 2020, Art. no. 136464, doi: 10.1016/j.electacta.2020.136464.

[24] D. Yang, H. Garg, and M. Andersson, "Numerical simulation of two-phase flow in gas diffusion layer and gas channel of proton exchange membrane fuel cells," *Int. J. Hydrogen Energy*, vol. 48, no. 41, pp. 15677–15694, May 2023, doi: 10.1016/j.ijhydene.2023.01.013.

[25] H. Xu, M. Bührer, F. Marone, T. J. Schmidt, F. N. Büchi, and J. Eller, "Fighting the noise: Towards the limits of subsecond X-ray tomographic microscopy of PEFC," *ECS Meeting Abstr.*, vol. 2, p. 1429, Sep. 2017, doi: 10.1149/ma2017-02/32/1429.

[26] H. Yuan, R. Du, X. Wang, X. Wei, and H. Dai, "Advanced online broadband impedance spectrum acquisition of fuel cells by S-transform," *IEEE Trans. Ind. Electron.*, vol. 70, no. 4, pp. 3740–3750, Apr. 2023, doi: 10.1109/TIE.2022.3177814.

[27] V. S. Bethapudi et al., "Hydration state diagnosis in fractal flow-field based polymer electrolyte membrane fuel cells using acoustic emission analysis," *Energy Convers. Manage.*, vol. 220, Sep. 2020, Art. no. 113083, doi: 10.1016/j.enconman.2020.113083.

[28] V. S. Bethapudi, G. Hinds, P. R. Shearing, D. J. L. Brett, and M.-O. Coppens, "Dynamic acoustic emission analysis of polymer electrolyte membrane fuel cells," *Energy Adv.*, vol. 1, no. 5, pp. 258–268, 2022, doi: 10.1039/d2ya00037g.

[29] Z. J. Jiao, X. Y. Huang, and N.-T. Nguyen, "Scattering and attenuation of surface acoustic waves in droplet actuation," *J. Phys. A, Math. Theor.*, vol. 41, no. 35, Sep. 2008, Art. no. 355502, doi: 10.1088/1751-8113/41/35/355502.

[30] J. Sablowski, Z. Zhao, and C. Kupsch, "Ultrasonic guided waves for liquid water localization in fuel cells: An ex situ proof of principle," *Sensors*, vol. 22, no. 21, p. 8296, Oct. 2022, doi: 10.3390/s22218296.

[31] R. Quintero and F. Simonetti, "Rayleigh wave scattering from sessile droplets," *Phys. Rev. E, Stat. Phys. Plasmas Fluids Relat. Interdiscip. Top.*, vol. 88, no. 4, pp. 1–13, Oct. 2013, doi: 10.1103/PhysRevE.88.043011.

[32] S. Tsunogaya and J. Kondoh, "Observation of reflected and transmitted waves caused by acoustic streaming in droplet on surface acoustic waves devices," *Jpn. J. Appl. Phys.*, vol. 57, Apr. 2018, Art. no. 07LD03.

[33] Z. Su and L. Ye, "Fundamentals and analysis of lamb waves," in *Proc. Identification of Damage Using Lamb Waves: From Fundamentals to Applications*. London, U.K.: Springer, 2009.

[34] P. C. Okonkwo et al., "A review of bipolar plates materials and graphene coating degradation mechanism in proton exchange membrane fuel cell," *Int. J. Energy Res.*, vol. 46, no. 4, pp. 3766–3781, Mar. 2022, doi: 10.1002/er.7428.

[35] S. Karimi, N. Fraser, B. Roberts, and F. R. Foulkes, "A review of metallic bipolar plates for proton exchange membrane fuel cells: Materials and fabrication methods," *Adv. Mater. Sci. Eng.*, vol. 2012, pp. 1–22, Jan. 2012, doi: 10.1155/2012/828070.

[36] G. Palumbo and A. Piccininni, "Numerical-experimental investigations on the manufacturing of an aluminium bipolar plate for proton exchange membrane fuel cells by warm hydroforming," *Int. J. Adv. Manuf. Technol.*, vol. 69, nos. 1–4, pp. 731–742, Oct. 2013, doi: 10.1007/s00170-013-5047-1.

[37] K. I. Jeong, J. Oh, S. A. Song, D. Lee, D. G. Lee, and S. S. Kim, "A review of composite bipolar plates in proton exchange membrane fuel cells: Electrical properties and gas permeability," *Composite Struct.*, vol. 262, Apr. 2021, Art. no. 113617, doi: 10.1016/j.compstruct.2021.113617.

[38] *Material Library*. Accessed: Feb. 1, 2023. [Online]. Available: https://www.comsol.com/material-library

[39] K. Mäder et al., "Phased array ultrasound system for planar flow mapping in liquid metals," *IEEE Trans. Ultrason., Ferroelectr., Freq. Control*, vol. 64, no. 9, pp. 1327–1335, Sep. 2017, doi: 10.1109/TUFFC.2017.2693920.

[40] Y. Yu, Q. Xiong, Z.-S. Ye, X. Liu, Q. Li, and K. Wang, "A review on acoustic reconstruction of temperature profiles: From time measurement to reconstruction algorithm," *IEEE Trans. Instrum. Meas.*, vol. 71, pp. 1–24, 2022, doi: 10.1109/TIM.2022.3203097.

[41] B. Liu, K.-J. Xu, L.-B. Mu, and L. Tian, "Echo energy integral based signal processing method for ultrasonic gas flow meter," *Sens. Actuators A, Phys.*, vol. 277, pp. 181–189, Jul. 2018, doi: 10.1016/j.sna.2018.05.019.

[42] M. Andersson et al., "Modeling and synchrotron imaging of droplet detachment in gas channels of polymer electrolyte fuel cells," *J. Power Sources*, vol. 404, pp. 159–171, Nov. 2018, doi: 10.1016/j.jpowsour.2018.10.021.

[43] M. El Mountassir, S. Yaacoubi, and F. Dahmene, "Reducing false alarms in guided waves structural health monitoring of pipelines: Review synthesis and debate," *Int. J. Pressure Vessels Piping*, vol. 188, Dec. 2020, Art. no. 104210, doi: 10.1016/j.ijpvp.2020.104210.

[44] R. Gorgin, Y. Luo, and Z. Wu, "Environmental and operational conditions effects on Lamb wave based structural health monitoring systems: A review," *Ultrasonics*, vol. 105, Jul. 2020, Art. no. 106114, doi: 10.1016/j.ultras.2020.106114.

[45] O. Putkis and A. J. Croxford, "Continuous baseline growth and monitoring for guided wave SHM," *Smart Mater. Struct.*, vol. 22, no. 5, May 2013, Art. no. 055029, doi: 10.1088/0964-1726/22/5/055029.

[46] I. S. Hussaini and C.-Y. Wang, "Visualization and quantification of cathode channel flooding in PEM fuel cells," *J. Power Sources*, vol. 187, no. 2, pp. 444–451, Feb. 2009, doi: 10.1016/j.jpowsour.2008.11.030.

[47] N. Ibrahim-Rassoul, E. K. Si-Ahmed, A. Serir, A. Kessi, J. Legrand, and N. Djilali, "Investigation of two-phase flow in a hydrophobic fuel-cell micro-channel," *Energies*, vol. 12, no. 11, 2019, doi: 10.3390/en12112061.

[48] P. Schmitt, "Optical versus acoustic turbidity in heavy loaded flows," in *Proc. 11th Int. Symp. Ultrason. Doppler Methods Fluid Mech. Fluid Eng.*, Sep. 2018, pp. 5–8.

[49] *NDT Wedges*. Accessed: Aug. 20, 2023. [Online]. Available: https://www.acoustics.co.uk/product/ndt-wedges/

[50] J. Eller and F. N. Bu, "Polymer electrolyte fuel cell performance degradation at different synchrotron beam intensities," *J. Synchrotron Radiat.*, vol. 21, no. 1, pp. 82–88, 2014, doi: 10.1107/S1600577513025162.

[51] J. Mitzel et al., "Fault diagnostics in PEMFC stacks by evaluation of local performance and cell impedance analysis," *Fuel Cells*, vol. 20, no. 4, pp. 403–412, Aug. 2020, doi: 10.1002/fuce.201900193.

[52] J. Kuo, A. Baskota, S. Zimmerman, F. Hay, S. Pethybridge, and A. Lal, "Gigahertz ultrasonic imaging of nematodes in liquids, soil, and air," in *Proc. IEEE Int. Ultrason. Symp.*, Sep. 2021, pp. 2021–2024.

[53] J. Yu, L. Lavery, and K. Kim, "Super-resolution ultrasound imaging method for microvasculature in vivo with a high temporal accuracy," *Sci. Rep.*, vol. 8, no. 1, pp. 1–11, Sep. 2018, doi: 10.1038/s41598-018-32235-2.

[54] Y. Li et al., "Incorporating the image formation process into deep learning improves network performance," *Nature Methods*, vol. 19, no. 11, pp. 1427–1437, Nov. 2022, doi: 10.1038/s41592-022-01652-7.

[55] S. Cheng et al., "Optimal warm-up control strategy of the PEMFC system on a city bus aimed at improving efficiency," *Int. J. Hydrogen Energy*, vol. 42, no. 16, pp. 11632–11643, Apr. 2017, doi: 10.1016/j.ijhydene.2017.02.203.

[56] X. Chen et al., "Temperature and voltage dynamic control of PEMFC stack using MPC method," *Energy Rep.*, vol. 8, pp. 798–808, Nov. 2022, doi: 10.1016/j.egyr.2021.11.271.

[57] A. H. Hosseinloo and M. M. Ehteshami, "Shock and vibration effects on performance reliability and mechanical integrity of proton exchange membrane fuel cells: A critical review and discussion," *J. Power Sources*, vol. 364, pp. 367–373, Oct. 2017, doi: 10.1016/j.jpowsour.2017.08.037.

[58] X. Xie et al., "Investigation of mechanical vibration effect on proton exchange membrane fuel cell cold start," *Int. J. Hydrogen Energy*, vol. 45, no. 28, pp. 14528–14538, May 2020, doi: 10.1016/j.ijhydene.2020.03.181.

[59] C. Liu, J. B. Harley, M. Bergés, D. W. Greve, and I. J. Oppenheim, "Robust ultrasonic damage detection under complex environmental conditions using singular value decomposition," *Ultrasonics*, vol. 58, pp. 75–86, Apr. 2015, doi: 10.1016/j.ultras.2014.12.005.

Zehua Dou (Graduate Student Member, IEEE) received the M.Sc. degree in micro and nanosystems from TU Chemnitz, Chemnitz, Germany, in 2019.

Afterward, he worked at the Leibniz Institute for Solid State and Materials Research Dresden (Leibniz IFW Dresden), Dresden, Germany. Since 2022, he has been an Academic Staff Member of the Laboratory for Measurement and Sensor System Techniques (MST), TU Dresden, Dresden. His research topic focuses on ultrasonic technologies for green hydrogen energy.

Bowen Fang received the B.Sc. degree in mechanical engineering from the Shanghai University of Engineering Science, Shanghai, China, in 2016. He is currently pursuing the M.Sc. degree in mechatronics with TU Dresden, Dresden, Germany.

In 2022, he joined the Laboratory for Measurement and Sensor System Technique (MST), TU Dresden, where he is currently working on his Diploma thesis. His research interests focus on control strategies and finite element method (FEM) simulations for MEMS sensors and actuators.

Laura Tropf received the B.Sc. degree in physics from the University of Rostock, Rostock, Germany, in 2011, the M.Sc. degree in physics from the University of Bremen, Bremen, Germany, in 2014, and the Ph.D. degree from the University of St Andrews, St Andrews, U.K., in 2019.

After having worked in the optical industry, she joined the Hydrogen and Fuel Cell Centre, ZBT GmbH, Duisburg, Germany, as a Staff Scientific Member, in 2020. For her thesis, she investigated strong light–matter interaction between cavity photons and organic semiconductors. Her current research focuses on laser-optical flow measurements for graphene synthesis and fuel-cell-related X-ray microscopy.

Harry Hoster received the M.Sc. degree in physics from the University of Bonn, Bonn, Germany, in 1996, with a special focus on imaging methods in medicine and surface science, the Ph.D. degree in fuel-cell-related surface science from the University of the Federal Armed Forces, Munich, Germany, in 2001, and the Habilitation degree in physical chemistry from Ulm University, Ulm, Germany, in 2010.

He accepted a Professor position in electrochemical energy storage at Technical University Munich, Munich, in 2010, and he became the Scientific Director and a Principal Investigator of the TUM CREATE Research Program on Electric Vehicles in Singapore. From 2015 to 2021, he was a Professor of physical chemistry and the Director of Energy Lancaster at Lancaster University, Lancaster, U.K. In 2021, he took over as the Chair of energy technology at University Duisburg-Essen, Duisburg, Germany, and he became the Scientific Director of the Hydrogen and Fuel Cell Centre, ZBT GmbH, Duisburg.

Hagen Schmidt (Member, IEEE) received the Diploma degree in electronics and the Ph.D. degree in electrical engineering from the Dresden University of Technology (TUD), Dresden, Germany, in 1992 and 2005, respectively.

He was with the Central Research Division, Robert Bosch GmbH, Stuttgart, Germany, and also with Vectron International GmbH, Teltow, Germany. In 1996, he joined the Leibniz Institute for Solid State and Materials Research, Dresden, where he is currently involved in the research on surface dynamics. Since its foundation in 2013, he has been the Co-Leader of SAWLab Saxony, Dresden. His current research interests include surface acoustic wave (SAW)-based sensors and actuators, e.g., for harsh environments and acoustofluidics, respectively, as well as high-precision microacoustic characterization of crystalline materials and thin-film systems.

Jürgen Czarske (Senior Member, IEEE) is currently the Director, a Chair Professor, and a Senator of TU Dresden, Dresden, Germany, where he is also the Director of the Competence Center Biomedical Computational Laser Systems (BIOLAS). He has authored or coauthored around 1000 articles and conference papers and has over 30 issued patents.

Prof. Czarske is a fellow of OPTICA, Society of Photo-Optical Instrumentation Engineers (SPIE), European Optical Society (EOS), Institute of Physics (IOP), and Institution of Engineering and Technology (IET). His awards include the 2008 Berthold Leibinger Innovation Prize, 2019 OPTICA Joseph-Fraunhofer-Award/Robert M. Burley Prize, 2020 Laser Instrumentation Award of the IEEE Photonics Society, 2020 and 2021 SPIE Community Champion for volunteer activities, and 2022 SPIE Chandra S. Vikram Award in Optical Metrology. Over 80 scientific prizes and honors were awarded to staff and students of his laboratory in the last 15 years. He is an Associate Editor of JEOS (RP) and LAM (Nature), and a Vice President of the International Commission for Optics (ICO). The talent cultivation plays an important role at his chair. He is an Advisor of the SPIE-OPTICA Student Chapter Dresden.

David Weik (Graduate Student Member, IEEE) received the Diploma degree in electrical engineering from Technische Universität Dresden (TU Dresden), Dresden, Germany, in 2017, with a focus on information technology and signal processing.

He worked at the Department of Medical Engineering, Fraunhofer Institute for Machine Tools and Forming Technology IWU, Dresden. Since 2019, he has been a Research Fellow with the Laboratory of Measurement and Sensor System Techniques, Ultrasound Metrology Group, TU Dresden. His current research interests include the application of adaptive sound fields in ultrasound-based flow instrumentation, especially for research in liquid metal fluid dynamics.